



Nanoelectronics enabled chronic multimodal neural platform in a mouse ischemic model

Lan Luan^{a,b,*}, Colin T. Sullender^a, Xue Li^a, Zhengtuo Zhao^a, Hanlin Zhu^a, Xiaoling Wei^a, Chong Xie^{a,**}, Andrew K. Dunn^{a,*}

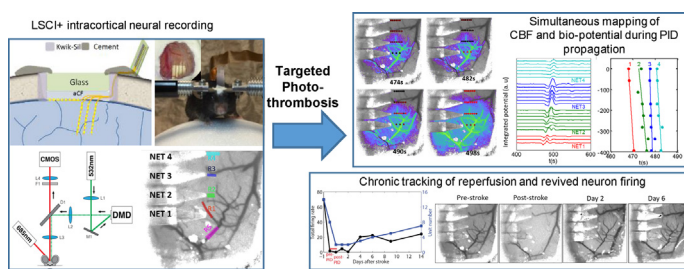
^a Department of Biomedical Engineering, The University of Texas at Austin, United States

^b Department of Physics, The University of Texas at Austin, United States

HIGHLIGHTS

- Arrays of ultra-flexible neural electrodes for single-unit neural recording at multiple cortical depths and locations.
- Lase speckle contrast imaging of cerebral blood flow (CBF) in the same brain region as neural recording.
- Targeted photothrombosis to induce stroke with fine control of lesion size and location.
- Spatiotemporally resolved, simultaneous mapping of the neural and hemodynamic signatures of peri-infarct depolarization.
- Longitudinal tracking of single-unit firing and CBF after the initial ischemia insult.

GRAPHICAL ABSTRACT



ARTICLE INFO

Article history:

Received 6 September 2017

Received in revised form

22 November 2017

Accepted 1 December 2017

Keywords:

Neural electrodes
Functional imaging
Electrophysiology
Multimodal
Hemodynamics
Stroke

ABSTRACT

Background: Despite significant advancements of optical imaging techniques for mapping hemodynamics in small animal models, it remains challenging to combine imaging with spatially resolved electrical recording of individual neurons especially for longitudinal studies. This is largely due to the strong invasiveness to the living brain from the penetrating electrodes and their limited compatibility with longitudinal imaging.

New method: We implant arrays of ultraflexible nanoelectronic threads (NETs) in mice for neural recording both at the brain surface and intracortically, which maintain great tissue compatibility chronically. By mounting a cranial window atop of the NET arrays that allows for chronic optical access, we establish a multimodal platform that combines spatially resolved electrical recording of neural activity and laser speckle contrast imaging (LSCI) of cerebral blood flow (CBF) for longitudinal studies.

Results: We induce peri-infarct depolarizations (PIDs) by targeted photothrombosis, and show the ability to detect its occurrence and propagation through spatiotemporal variations in both extracellular potentials and CBF. We also demonstrate chronic tracking of single-unit neural activity and CBF over days after photothrombosis, from which we observe reperfusion and increased firing rates.

Comparison with existing method(s): This multimodal platform enables simultaneous mapping of neural activity and hemodynamic parameters at the microscale for quantitative, longitudinal comparisons with minimal perturbation to the baseline neurophysiology.

* Corresponding authors at: Lan Luan: 107 W Dean Keeton Street, BME 4.202B; Andrew Dunn: 107 W Dean Keeton Street, BME 4.202I.

** Corresponding author at: 107 W Dean Keeton Street, BME 5.2020, United States.

E-mail addresses: lluan@utexas.edu (L. Luan), chongxie@utexas.edu (C. Xie), adunn@utexas.edu (A.K. Dunn).

Conclusion: The ability to spatiotemporally resolve and chronically track CBF and neural electrical activity in the same living brain region has broad applications for studying the interplay between neural and hemodynamic responses in health and in cerebrovascular and neurological pathologies.

© 2017 Elsevier B.V. All rights reserved.

1. Introduction

Because brain function and dysfunction depend on the delicate balance between substrate delivery through blood flow and energy demands imposed by neural activity (Attwell et al., 2010), simultaneous mapping of neural activity and hemodynamics in behaving brain is crucial to the understanding of brain functionality in health (Fox and Raichle, 1986), as well as the damaging mechanism and recovery of neurovascular diseases (Bundo et al., 2002). In particular, the characteristics and the impacts of ischemic stroke are multifaceted in nature, in which disrupted cerebral vascular blood flow negatively impacts the neuronal activity and tissue outcome (Zhang and Murphy, 2007; Strong et al., 2007; Nakamura et al., 2010). Moreover, although the effects of ischemic stroke in both patients and experimental animal models are apparent only minutes after blood flow is reduced (Zhang et al., 1997; Hainsworth and Markus, 2008), the progression of ischemia lasts for several days after the initial insult (Hartings et al., 2003; Fabricius et al., 2006), and the functional recovery of the injured brain continues for months and longer (Murphy and Corbett, 2009). While extensive research has been done on the progression of brain injury in focal stroke at the acute phases in small animal models (Zhang and Murphy, 2007; Shin et al., 2006; Jones et al., 2008; Brown et al., 2009), the progression of ischemic conditions and recovery into chronic time scales are understudied (Dirnagl et al., 1999), in large part due to a lack of methods capable of quantifying multiple neurophysiological parameters simultaneously in behaving brains with sufficient spatial resolution over periods of weeks to months.

In vivo optical imaging has been a major tool for studying stroke models in small animals (Zhang and Murphy, 2007; Nakamura et al., 2010; Jones et al., 2008; Strong et al., 2006; Brown et al., 2007; Sakadzic et al., 2010) owing to its unique strength including high spatial resolution, reasonable penetration depth, and high specificity and sensitivity to various structural and functional imaging parameters. For example, two-photon (2P) microscopy have been routinely used for imaging subsurface microvascular structures (Nishimura et al., 2006; Schaffer and et al., 2006), neuron (Li and Murphy, 2008) and glial (Davalos et al., 2005) morphology, for quantitative, depth-resolved measurement of red blood cell (RBC) flux and velocities (Kamoun et al., 2010), for phosphorescence lifetime imaging of pO₂ that determines the absolute oxygen concentration with subcellular resolution (Rumsey et al., 1988), and for voltage-sensitive dye (Brown et al., 2009) and calcium imaging (Winship and Murphy, 2008) of individual neuron activities. In particular, laser speckle flowmetry (LSF) is used to measure cortical perfusion (Strong et al., 2006) and cerebral blood flow (CBF) (Dunn et al., 2001) with high temporal and spatial resolution. Laser speckle contrast imaging (LSCI) is used as a cost-effective method for visualizing and quantifying neurovascular blood flows particularly in small animals (Dunn et al., 2001; Li et al., 2006). Multi-exposure speckle imaging (MESI), a refined method of LSCI to eliminate artifacts, allows for quantitative measurement of CBF for longitudinal studies and cross-animal comparisons (Kazmi et al., 2013; Kazmi et al., 2015; Schrandt et al., 2015). In contrast, electrical recording in stroke models mostly relies on techniques developed decades ago that offers one or few recording sites either subdural (Nakamura et al., 2010; Strong et al., 2002; Dohmen et al., 2008; Dreier et al., 2006) or intra-cortical (Jeffcote et al., 2014), with electrode dimensions and distance from the infarct often both on millimeter scales,

lacking the necessary spatial resolution and specificity. In the effort of multi-modality investigation, transparent electrode arrays were used for combined neuroimaging and recording from the surface of the brain (Park et al., 2014) or on tissue slices (Kuzum et al., 2014). The spatiotemporal relationship between cortical slow potential shifts and CBF changes in response to peri-infarct depolarizations (PIDs) was studied using one or a few electrodes simultaneously with LSF or LSCI in rodents (Shin et al., 2006) and cats (Strong et al., 2007). However, the study was only carried out acutely without the ability to record and track single-unit neural activity.

The challenge for integrating high-resolution electrical recording with optical techniques chronically lies on the fundamental challenges of tissue long-term biocompatibility using intracortical microelectrodes, which is the only method to record action potentials from individual neurons at sub-milliseconds temporal resolution. Conventional electrodes generate substantial tissue damage both acutely (Potter et al., 2012; Kozai et al., 2014) and chronically (Rousche and Normann, 1998; Polikov et al., 2005), resulting in sustained tissue reaction near the implants including continuous leakage of blood-brain barrier, neuronal death and glial scar formation (Seymour and Kipke, 2007; Zhong and Bellamkonda, 2008; Jeong et al., 2015). These reactions generate a probe-induced damage zone in brain, which affects the viability of experimental models if the electrodes were placed within or in close vicinity of the ischemic penumbra. Furthermore, conventional microelectrodes are constructed on rigid material such as metal and silicon. Their long-term implantation and skull fixation geometrically affect chronic optical access to the same brain region (Kozai et al., 2016).

We successfully resolved both the challenges of tissue-compatibility and chronic optical access by our recent development of a novel type of ultraflexible neural electrodes, the nanoelectronic thread (NET) (Luan et al., 2017). We demonstrated that NETs form reliable, glial scar free neural-probe interface, which was verified by chronic neural recordings and comprehensive tissue-probe interface characterizations. Longitudinal *in vivo* two-photon imaging and postmortem histological analysis revealed seamless integration of NET probes with the local cellular and vasculature networks. In particular, we observed fully recovered capillaries with intact blood brain barrier, and complete absence of chronic neuronal degradation and glial scar (Luan et al., 2017). In this study, we combine LSCI of relative CBF (rCBF) with electrical recording of neural activity using NETs at different locations and cortical depths in a mouse stroke model, in which we are also able to induce targeted photothrombotic occlusions within individual vessels with a fine control over lesion location and size (Ponticorvo and Dunn, 2010; Sullender et al., 2017). We demonstrate simultaneous mapping of neural activity and rCBF beyond the acute phase of stroke, including the progression of ischemia, and the reperfusion and revival of neural activity over days and longer.

2. Materials and methods

2.1. Ultraflexible NET electrodes fabrication and preparation

The NET brain probes were fabricated using specialized fabrication methods similar to previously reported (Luan et al., 2017; Tian

et al., 2012; Xie et al., 2015). The multi-layer probes were fabricated using photolithography on a nickel metal release layer deposited on a silicon substrate (900 nm SiO₂, n-type 0.005 V cm, University Wafer, Inc. MA, USA). SU-8 photoresist (SU-8 2000.5, MicroChem Corp. MA, USA), which offers excellent tensile strength, ease of fabrication and demonstrated durability in ultra-thin structures (Tian et al., 2012; Xie et al., 2015; Liu et al., 2015), was used to construct the insulating layers. The total thickness of NETs used in this study is about 1 μm, which offers ultraflexibility and is sufficient to prevent leakage over long-term implantation (Luan et al., 2017). Platinum or gold was used for electrodes (size: 30 μm × 30 μm for NET-50) and interconnects, respectively, both with a thickness of 100 nm. After fabrication, a 33-pin FFC/FPC connector (series 502598, Molex, IL, USA) was mounted on the matching contact pads on the Si substrate. The implantable section of the probe was then soaked in nickel etchant (TFB, Transene Inc., MA, USA) for 2–4 h at 25 °C to release the free-standing portion of the probe, whereas the contact region remained attached to the substrate. The substrate was cleaved to the desired length before implantation. The released sections of NETs were attached onto shuttle devices made of carbon fibers or tungsten microwires fixed on a Si piece at matching pitch using bio-dissolvable adhesive PEG (4000 g/mol, Fisher Scientific, PA, USA). The Si base-piece of the shuttle device was also glued on the silicon substrate of the NETs using PEG. Both the NETs and shuttle devices were soaked in sterile 70% ethanol before assembling for sterilization.

2.2. Animal preparation

Mice (Wild-type, C57B6, male, 25–30 g, Taconic, Hudson, NY, USA) were anesthetized with medical O₂ vaporized isoflurane (3%) in an induction chamber and then placed supine in a stereotaxic frame (Kent Scientific, Connecticut, USA) in via nose-cone inhalation of medical O₂ vaporized isoflurane (1.5–2%). Carprofen (5 mg/kg) and dexamethasone (2 mg/kg) were administrated subcutaneously to reduce inflammation of the brain during the craniotomy and implantation procedure. Body temperature was maintained at 37 °C with a feedback heat pad (DCTemperature Controller, FHC, Bowdoin, ME, USA). Arterial oxygen saturation, heart rate, and breath rate were monitored via pulse oximetry (MouseSTAT, Kent Scientific, Connecticut, USA). The scalp was shaved and resected to expose skull between the bregma and lambda cranial coordinates. A thin layer of cyanoacrylate (Vetbond, 3 M, MN, USA) was applied to exposed skull to facilitate the adhesion of dental cement during a later step. A square or circular portion of skull (at least 3 mm × 3 mm) was removed with a dental drill (Ideal Microdrill, 0.8 mm burr, Fine Science Tools, CA, USA) under constant sterile artificial cerebrospinal fluid (buffered pH 7.4) perfusion. Dura mater was partially removed to open a narrow slit for NET implantation. The partial dura removal on experienced hands did not induce additional damage to the nearby vasculature (Luan et al., 2017). Before NET implantation, a bare Ag wire was inserted into the contralateral hemisphere of the brain as the grounding reference for later electrical recording. The NET-shuttle assembly was delivered to the target cortical depth and location using a manual manipulator mounted on the stereotaxic frame. After PEG dissolved under constant sterile artificial cerebrospinal fluid perfusion for a few minutes, the shuttle device was retracted out the brain tissue using the second manual manipulator on the stereotaxic frame. The deliver angle was about 45 deg from perpendicular to the brain surface. The implanted electrodes were typically evenly distributed from brain surface to cortical depth of 400 μm. In some animals, some electrodes were placed on the brain surface using as μECoG electrodes. A 3–5 mm round or square cover glass (#1, World Precision Instruments, Sarasota, FL, USA) was placed over the exposed brain with a layer of artificial cere-

brospinal fluid between the two. Gentle pressure was applied to the cover glass while the space between the coverslip and the remaining skull was filled with Kwik-sil adhesive (World Precision Instruments, FL, USA). An initial layer of C&B-Metabond (Parkell Inc, NY, USA) was applied over the cyanoacrylate and the Kwik-sil. This process ensured a sterile, air-tight seal around the craniotomy and allowed for restoration of intracranial pressure (Fig. 1A). A second layer of Metabond was used to cement the coverslip and the NET carrier chip to the skull. A final layer of Metabond was used to cement a customized titanium head-plate for later head-constrained measurements. Animals were allowed to recover from the surgery and monitored for cranial window integrity and behavior normality for eight weeks prior to the multimodal study. Awake, head-constrained electrophysiological recording were perform when the animal ran on a customized treadmill (Fig. 1B,C). All subsequent imaging sessions were conducted using medical air with 1.5% vaporized isoflurane to ensure the animal maintained full immobility during imaging in a compact stereotaxic frame (Narishige Scientific Instrument Lab, Tokyo, Japan). All experiments were approved by the Institutional Animal Care and Use Committee (IACUC) at The University of Texas at Austin and comply with the National Institutes of Health guide for the care and use of Laboratory animals.

2.3. Imaging instrumentation and targeted photothrombosis

A schematic of the imaging system is presented in Fig. 1D. Laser speckle contrast imaging (LSCI) of blood flow was performed using a 685 nm laser diode (50 mW) illuminating the craniotomy at an oblique angle. The backscattered laser light was relayed to a CMOS camera (acA1300-60gmNIR, 1280 × 1024 pixels, Basler AG, Germany) with 2× magnification and acquired at 60-frames-per-second with 5 ms exposure time using custom software.

A digital micromirror device (DMD) was used to induce user-defined photothrombotic occlusions (Ponticorvo and Dunn, 2010; Sullender et al., 2017) in the cortical vasculature using rose bengal, a fast-clearing photothrombotic agent that photochemically triggers localized clot formation upon irradiation with green light. A DMD is an optical semiconductor that consists of a two-dimensional array of thousands of individually addressable mirrors that can be tilted to spatially modulate light. A DLP LightCrafter Evaluation Module (Texas Instruments, Dallas, TX, USA) was modified to expose the bare DMD (DLP3000, 608 × 684 micromirrors, 7.6 μm pitch) for illumination. The projected DMD pattern was co-registered with the LSCI camera via an affine image transformation (Fig. 1E). This allowed for the selection of arbitrarily-shaped regions of interest using the LSCI imagery, which were then transformed into DMD coordinate space and loaded onto the device. The DMD allows for the targeting of individual vessels for occlusion while minimizing exposure in the surrounding parenchyma. Rose bengal was injected intravenously (50 μL, 15 mg/mL) and the target vessels exposed to DMD-patterned 532 nm CW laser light for 5 min. Descending arterioles were the primary target because they serve as bottlenecks in the cortical oxygen supply. Real-time LSCI was used to monitor clot formation within the targeted area and control the progression of the occlusion.

2.4. Electrophysiological recording

Electrical recording were performed before the imaging sessions for baseline, simultaneously during imaging and photothrombosis, and independent of imaging sessions after photothrombosis. Voltage signals from the NEC devices were amplified and digitized using a 32-channel RHD 2132 evaluation system (Intan Technologies, Los Angeles, CA, US) with the bare Ag in the contralateral hemisphere of the brain as the grounding reference. The sampling

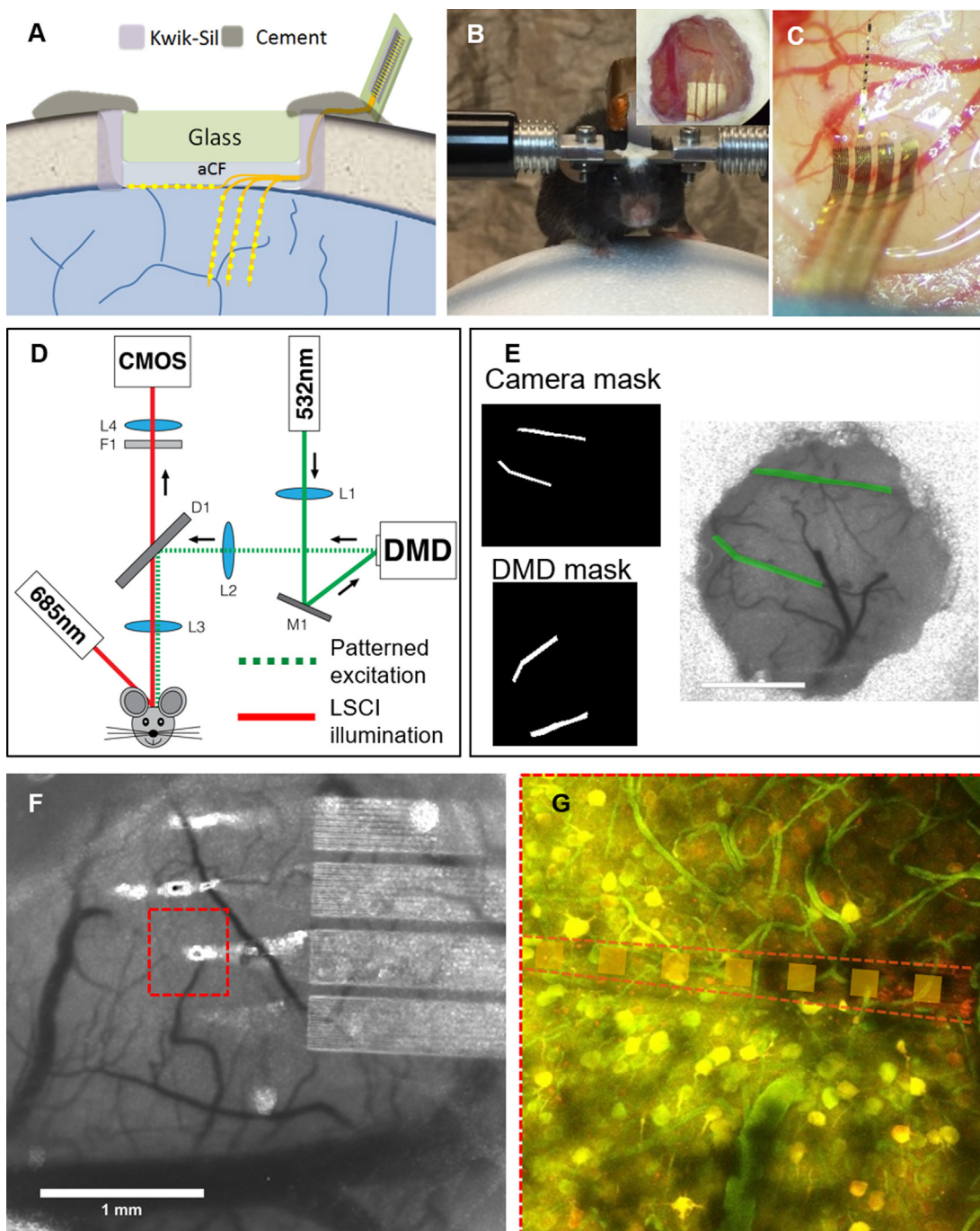


Fig. 1. Nanoelectronic thread enabled multimodal neural platform. A: Schematic of skull fixation showing the chronic optical access and NET implantation at the surface and cortical depth. Not drawn to scale. B: Photograph of a typical mouse with implanted NET probes and a glass window mounted on top on a customized treadmill for awake recording. Insets: zoom-in view of the glass window and the implanted NETs underneath it. C: photograph of a mouse brain showing that three shanks of NETs implanted intracortically and one on the surface. D: Schematic of the imaging system consist of a laser speckle imaging using 685 nm illumination and a diode lasers (532 nm) coupled with the DMD to provide structured illumination for targeted photothermolysis. E: Example of the image transformation used for DMD pattern projection that allows precise targeting of individual branches of arterioles. F: A representative LSCI near implanted NETs. G: Stacks of two-photon imaging showing little perturbation of the NET on local neuronal(yellow) and vascular (green) networks. Neurons are fluorescently labeled by virus transduction (turbo-RFP) during NET implantation. (For interpretation of the references to colour in this figure legend, the reader is referred to the web version of this article.)

rate was 20 kHz. In the detection of slow potential change during acute stroke, no additional filter was applied except a build-in high-pass filter at 0.5 Hz. When the recording was performed separately from imaging, mice were head constrained on a custom made treadmill to allow walking and running, and a 300 Hz high-pass and a 60 Hz notch filter were applied for single-unit recording. When the recording was performed simultaneously during imaging, mice were anesthetized using medical air with 1.5% vaporized isoflurane.

3. Experimental

During cranial surgery, we implanted NETs on the surface of and/or into the cortical regions of somatosensory and motor cortices (Fig. 1C) for $n=4$ mice. After allowing the animal to recover after cranial surgery for eight weeks, we performed baseline imaging to confirm the recovery of vasculature. As shown in the representative images in Fig. 1F,G, LSCI shows the normal surface

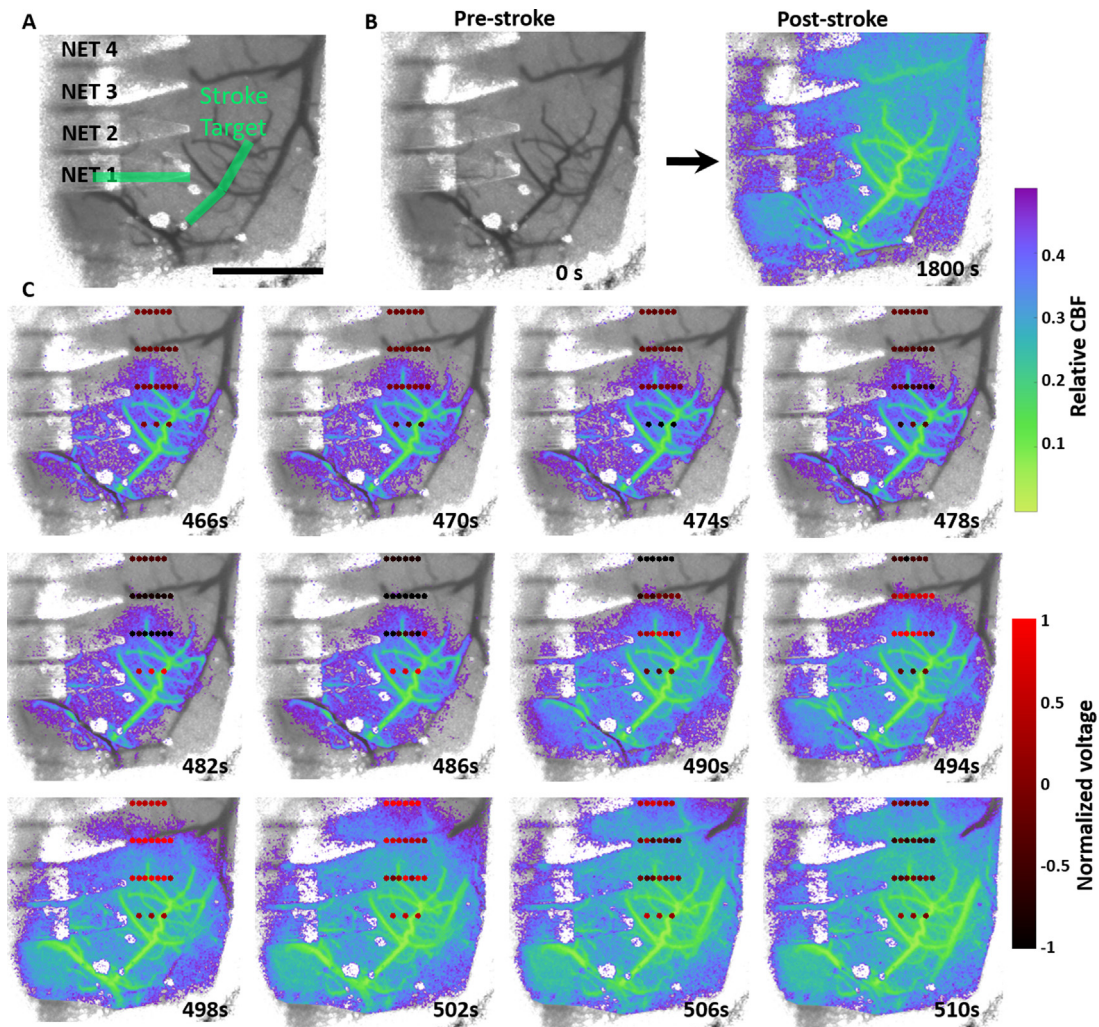


Fig. 2. Simultaneous mapping of relative CBF and cortical potential during a peri-infarct depolarization event. A: Baseline LSCI showing the location of NETs and the targeted arterioles for photothrombosis (green). Note that one of the arterioles is under the NET. B: LSCI of relative blood flow pre- and post-stroke induced by targeted photothrombosis under 532 nm illumination. C: An ischemia-induced peri-infarct depolarization event that results in significant changes in cortical potential and the expansion of blood flow deficit. The dots mark the locations of individual electrodes on the NETs and are color-coded by the normalized potential. (For interpretation of the references to colour in this figure legend, the reader is referred to the web version of this article.)

vasculature and rCBF near the NETs. Consistently, 2P imaging shows the normal morphology and density of vasculature and neurons near the implanted NET at subsurface. Baseline electrophysiological recording was also performed. The animal was then anesthetized and placed on a stereotaxic frame for the concurrent imaging and recording session in which photothrombosis was induced in target branches of surface vasculature while LSCI of rCBF and NET recording of neural activity were simultaneously performed. The targeted branches of arteriole were in close vicinity of the NETs to ensure that the multi-shank NET spanned from the ischemic core to penumbra. As shown in Fig. 2A, arterioles under the NETs can also be targeted for photothrombosis owing to the optical transparency of the NETs. The simultaneous recording and imaging sessions typically lasted for one hour. One or two peri-infarct depolarization(PID) events spontaneously occurred during this time, which induced significant changes both in blood flow and neural activity, and was recorded by LSCI and NET recording. To track the change of rCBF and neural activity chronically, follow-up recording sessions were performed on awake, head-constrained animal and LSCI sessions were performed on anesthetized animal for up to two weeks after the initial insult. In order to limit the stress and the dose of anesthesia on the post-stroke animals, the measurement duration

were short (10 mins for recording, 5 mins for imaging) and were performed once every few days.

4. Results

The progression of ischemia induced by targeted photothrombosis within one or few branches of descending arteriole was recorded with LSCI while the neural activity near the thrombosis was recorded with NET electrodes. Fig. 2 shows the hemodynamic and neural consequences of the targeted photothrombosis on one animal in which a 4-shank NET with 22 working electrodes was implanted intracortically in the mouse motor cortex. In Fig. 2A, the green overlay in the pre-photothrombotic frame depicts the arteriole branches illuminated with 532 nm laser light for 300 s. The remaining frames (Fig. 2B,C) show an overlay of relative blood flow baselined against pre-photothrombotic images. After illumination ceased at $t=300$ s, simultaneous imaging and recording of the post-photothrombosis hemodynamic and neural response continued for approximately 25 min. Although photothrombosis was contained to the targeted vessel as we previously demonstrated, by $t=1800$ s relative blood flow of most region under the cranial window had decreased to less than 40% of the baseline flow.

Fig. 2C depicts the propagation of an ischemia-induced depolarization event (Shin et al., 2006; Dreier, 2011) that occurred between $t=460\text{--}510\text{s}$. Color coded dots in **Fig. 2C** present the location and the recorded potential from NET electrodes and show a wave of cortical slow potential change propagating from bottom up across the NET electrode array. Accompanied with this neural response, a wave of blood flow reduction was seen spreading from bottom to up across the entire cranial window (Video 1). We note that there was time latency between the neural and hemodynamic response during the depolarization events: the cortical potential started to drop at $t=470\text{s}$ while the reduction of blood flow occurred later, which agreed with previous studies (Strong et al., 2007). The bio-potential NET recorded overshoot above baseline values after the decrease due to the ringing effect of the build-in high-pass filter at 0.5 Hz in our recording system (Gibbs, 1898). By $t=510\text{s}$ the depolarization event had subsided, the cortical potential recorded by all NET electrodes had returned to the baseline and the region experiencing reduced blood flow had also increased to include numerous surrounding vessels and parenchyma.

Relative CBF of regions of interest (ROIs) were also recorded. Consistent with the correlation between rCBF and neural potential changes throughout the entire field of view, relative flow from ROIs near the NET electrodes showed close spatial-temporal correlation with the potential changes. As shown in **Fig. 3**, rCBF measured at all ROIs decreased sharply in response to the potential change induced by the PID propagation. The onset of the rCBF decrease had time lag among ROIs (**Fig. 3C**), consistent with the propagation direction and speed of the PID observed from the full-field LSCI imaging series (**Fig. 2**). The PID induced potential changes were recorded in all channels, both in the raw signal (**Fig. 3D**) and in the integrated potential (**Fig. 3E**) which we computed from the raw potential to partially compensate for the high-pass filter on the AC-coupled amplifier (more discussions on the limitations of AC-coupled filter in the later sections). The neural response to the PID also showed lagged onset time of the potential change depending on the electrode's location and cortical depth (**Fig. 3E, F**). We obtained the surface propagation speed to be $v=5.6\text{ mm/min}$ using the top-most electrode of each shank at inter-shank spacing of $400\text{ }\mu\text{m}$, in good agreement with values of $2\text{--}7\text{ mm/min}$ reported in literature (Strong et al., 2007; Nakamura et al., 2010; Strong et al., 2006; Lauritzen, 1994; Woitzik et al., 2013). We obtained an averaged slope of $v_p=190\pm80\text{ }\mu\text{m/s}$ along depth, significantly larger than the surface propagation speed. The onset of decrease in blood flow lagged behind the decrease in neural potential by $12\text{--}16\text{s}$ (**Fig. 3G**, both were measured at 20% decrease), in agreement with previous results (Strong et al., 2007).

In addition to recording the slow potential change during the PID event, the intracortical microelectrodes on NETs also recorded action potentials from individual neurons. As shown in **Fig. 4A**, the photothrombosis itself did not result in significant change in the single-unit firing rates. However, all neurons were silenced when PID occurred, as they failed to maintain the resting membrane potential. After PID, most units did not fire action potentials until the end of the experiment, while three units were firing sparsely after more than 400 s of complete absence of unit activity. The neurons that fired post-PID were all recorded by electrodes on NET 4, which was the furthest away from the infarct core and had relatively weak suppression in CBF (**Fig. 3**). This is consistent with previous studies showing that neurons may remain viable at the acute phase in the ischemic penumbra at mild to moderate ischemic conditions.

Taking advantage of the chronic nature of the multimodal platform, we continued to follow neural activity and blood flow days after the photothrombosis, and compared with the pre-stroke baselines. Neural activity was recorded on awake animal except during the photothrombosis and subsequent 25 min, which was highlighted in red in **Fig. 4B**. Both the firing rates and the number of

units recorded by NET electrodes decreased to the minimum immediately after the PID events. While reperfusion in the lesion sites were observed at Day 2 (**Fig. 4C**) where most flow in the arteriole branch for photothrombosis had re-perfused, neural activity remained inactive as signified by the similarly low firing rates and unit numbers comparing with post-PID. By Day 6 the structure of the blood flow in the targeted arteriole had fully recovered to the pre-stroke baseline, whereas the number of recorded single-unit action potentials and the firing rates kept increasing until day 14 to a level that was still lower than the baseline. By day 14 no unit activity was detected by functioning electrodes on NET 1 and 2 where the tissue was in close proximity to the lesion sites and subjected to severe ischemia.

5. Discussion

Comparing with conventional microelectrodes that are made of opaque, rigid materials, the NET electrodes enable facile optical access to the same brain region for longitudinal in vivo studies due to their ultra-flexibility and optical transparency. Moreover, we demonstrate in this study that intracortical implantation of NET arrays in the vicinity of the lesion sites does not qualitatively affect the induction and the progression of the ischemic insult, nor the progressive reperfusion over days and longer. These results, combined with our previous study showing that the NET electrodes elicit little chronic tissue reactions including the complete absence of glial scar formation and leakage in BBB (Luan et al., 2017), suggest that NETs can be applied to the study of neurovascular disease models such as ischemic stroke model with minimal impacts on the baseline physiology. This work focuses on the technical demonstration of this longitudinal neural platform. The quantitative correlation between local CBF and neural activity from nearby neurons can be carefully evaluated using such a system on large number of animals.

The inter-shank spacing of the NETs was $400\text{ }\mu\text{m}$ so that the 4-shank 32-channel devices span 1.2 mm . Here we took advantages of targeted photothrombosis where we controlled the lesion size and location, and chose to target partial branches of arterioles near one NET shank. From our previous experience, such small occlusions typically lead to ischemic penumbra in mouse brain spanning $1\text{--}2\text{ mm}$ (Schrandt et al., 2015), matching the spatial distribution of the NET electrodes. The inter-shank spacing and the intra-shank distribution of NET electrodes can be adjusted for lesions of various sizes and severity.

The optical system uses inexpensive components such as diode lasers and a DMD. In particular, the DMD allows for targeted photothrombosis to create an extended occlusion within a branching arteriole. Comparing with previous techniques that either use broad illumination to occlude a large volume of vasculature (Watson et al., 1985) or highly focused light to occlude a single microvessel (Schaffer and et al., 2006), this system allows for fine control over the spatial characteristics of the stroke including size and location to possibly produce pathophysiologically relevant ischemic lesions.

Baseline and follow-up neural recording sessions in the current study were performed on head-constrained awake, behaving mice to eliminate the effect of anesthesia. However, isoflurane anesthesia was still used for imaging sessions and the simultaneous-imaging sessions, which may significantly affects systemic hemodynamics (Janssen et al., 2004) and neural activity, making it difficult for quantitatively tracking and comparison over longitudinal studies. In particular, the reduced neural activity during stroke-induction session compared with baseline was partially due to the effect of anesthesia, which is known to strongly suppress the firing rate and the number of spontaneously active

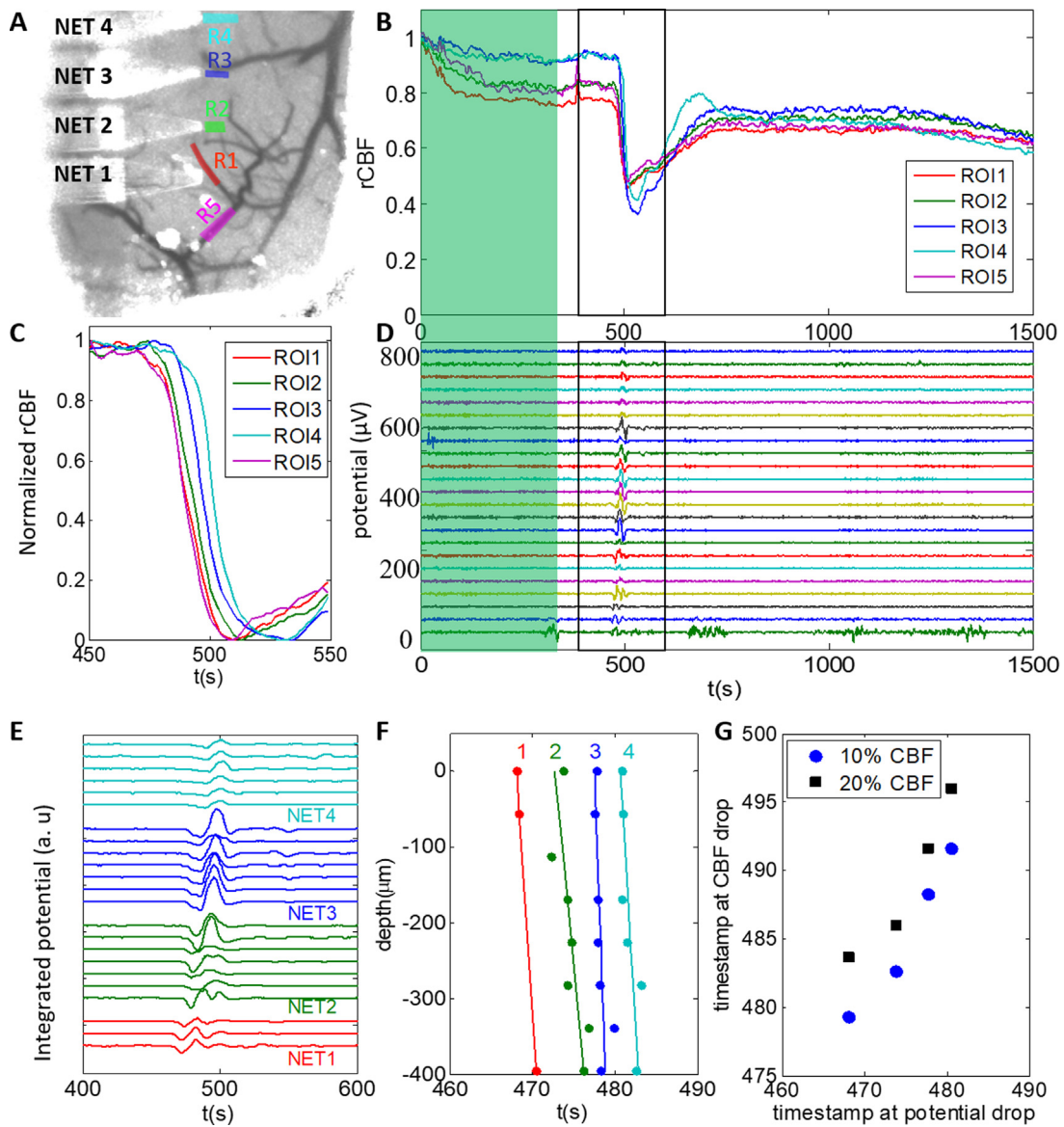


Fig. 3. Concurrent recording of neural potentials and rCBF at nearby locations. A: ROIs overlaid on pre-stroke LSCI. ROI1–4 are chosen next to the NET electrodes and ROI5 is chosen on the targeted arteriole for occlusion. B: rCBF of ROIs during photothrombosis (green shade) and subsequent 25 min, highlighting the drastic decrease in blood flow when PID occurred. C: rCBF baselined at $t = 450$ s showing the time latency of flow reduction among ROIs during the PID event. D: Neural potential recorded from 22 electrodes on 4 shanks of NETs during photothrombosis (green shade) and subsequent 25 min, highlighting the potential change when PID occurred. E: Neural potential changes near the PID event, showing time latency among different shanks and within individual shanks. F: The onset of the potential decrease at different shanks (labeled by the number atop) and depths. G: The time latency between neural potential decrease recorded by the topmost electrode on each shank and rCBF decrease. Two thresholds (10% and 20% decrease of CBF baselined at $t = 450$ s) were used. (For interpretation of the references to colour in this figure legend, the reader is referred to the web version of this article.)

neurons (Ferron et al., 2009). In addition, none of the neurons being recorded were active for a few hundreds of seconds after PID, which were likely due to the combined effects of ischemia and anesthesia. The implementation of an awake imaging setup would ameliorate this concern by completely eliminating the need for anesthesia during imaging and simultaneous imaging-recording sessions. The recording and imaging can potentially be performed on free-moving animals with some technical improvement using wireless and voluntary constrain techniques (Murphy et al., 2016).

In this study, AC-coupled amplifiers were used for NET recording, which allow for detection of spike activity but compromise the accuracy in detecting the DC potential shift induced by PIDs. In particular, although AC coupled potential showed strong correlation to the DC-coupled potential shift during PID (Hartings et al., 2006), it lacks quantitative accuracy in determining the value of the poten-

tial shift and its time duration. DC coupled amplifiers will improve the accuracy in detecting PID events (Hartings et al., 2006).

This study used single-exposure speckle imaging of relative blood flow, which provided limited accuracy in quantifying the flow for longitudinal study and cross-animal comparisons (Kazmi et al., 2013). The quantitative accuracy of blood flow measurements will be improved by MESI, which will allow for chronic tracking of blood flow in the ischemic brain (Kazmi et al., 2013; Kazmi et al., 2015; Schrandt et al., 2015). In addition, the DMD that enables targeted photothrombosis also allows for mapping of oxygenation (pO_2) at microscale and tens of ms temporal resolution (Sullender et al., 2017), which is more than sufficient for visualizing dynamic physiological events such PIDs. With straightforward modification, simultaneous mapping of pO_2 , hemoglobin oxygenation, blood flow, and neural activity can be achieved.

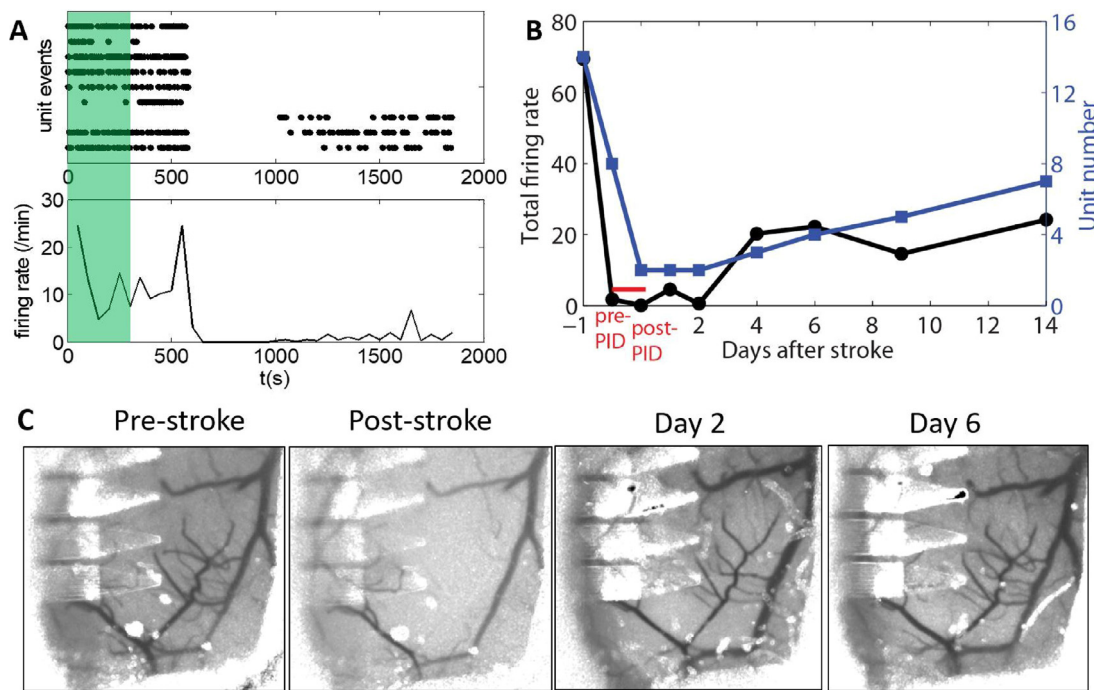


Fig. 4. Recovery of neural activity and reperfusion over days after photothrombosis. A: single-unit firing events plotted as dot (top) and firing rate per min (bottom) during photothrombosis (green shade) and subsequent 25 min. B: The total firing rate from all recorded units (left) and number of recorded units (right) as a functions of days after stroke. The 30 min session in A is divided to pre- and post- PID, both taken under anesthesia. C: Repeated LSCI at the same brain region showing progressive reperfusion of the occluded vessels after photothrombosis. (For interpretation of the references to colour in this figure legend, the reader is referred to the web version of this article.)

This work demonstrated the combination of two broad technical frameworks, neural recording using penetrating electrodes and optical imaging. The optical methods that can be combined with NET recording of neural electrical activity extend beyond imaging of hemodynamic parameters as demonstrated in the study. Because the cranial window preparation is commonly used for a variety of imaging methods at different length scales, their combination with electrical recording using NETs will create chronic multimodal neural platforms for a broad range of basic and applied neuroscience studies. For example, wide-field imaging of full-field neural activity (Murphy et al., 2016) can be combined with electrical recording of individual neurons in specific regions of interest in the investigation of neural plasticity due to experience or injury. Two-photon imaging of sub-surface Ca^{2+} transits (Winship and Murphy, 2008) or voltage-sensitive dye (Brown et al., 2009) can be combined with electrical recording of the same neuron to characterize both fluorescent intensity and the electrical waveform as a function of the numbers of action potentials generated from this neuron. Two-photon imaging of blood flow in capillaries (Schaffer and et al., 2006) in response to nearby neural activity can also be quantified to provide new microscopic information on neurovascular coupling.

6. Conclusions

We have presented a chronic multimodal neural platform that simultaneously maps relative cerebral blood flow with LSCI and neural activity using NET electrode array, both can be repeated for longitudinal studies over weeks and longer. We demonstrated the ability to induce targeted photothrombotic strokes within individual vessels in mouse cortex, to simultaneously map the change of neural activity and blood flow during an ischemic event, and to chronically track neural activity and blood flow during reperfusion that takes place days after the initial ischemic insult. This neural platform has broad applications for studying the progression and recovery of ischemic stroke, and other pathophysiological conditions in the brain.

sion and recovery of ischemic stroke, and other pathophysiological conditions in the brain.

Acknowledgements

We thank the Microelectronics Research Center at UT Austin for the microfabrication facility and support, and the Animal Resources Center at UT Austin for animal housing and care. This work was funded by National Institute of Neurological Disorders and Stroke through R21NS102964 (L.L.), R01NS102917 (C.X.), R01NS082518 (A.K.D.) and R01NS078791 (A.K.D.), by National Institute of Biomedical Imaging and Bioengineering through R01EB011556 (A.K.D.), by the American Heart Association through 14EIA18970041 (A.K.D.), by the Welch foundation Research grant #F-1941-20170325 (C.X.), by Department of Defense through Clinical and Rehabilitative Medicine Research Program under award no. W81XWH-16-1-0580 (C.X.), and by a UT BRAIN Seed grant award #365459 from the UT System Neuroscience and Neurotechnology Research Institute (L.L.).

Appendix A. Supplementary data

Supplementary data associated with this article can be found, in the online version, at <https://doi.org/10.1016/j.jneumeth.2017.12.001>.

References

- Attwell, D., et al., 2010. Glial and neuronal control of brain blood flow. *Nature* 468 (7321), 232–243.
- Brown, C.E., et al., 2007. Extensive turnover of dendritic spines and vascular remodeling in cortical tissues recovering from stroke. *J. Neurosci.* 27 (15), 4101–4109.
- Brown, C.E., et al., 2009. In vivo voltage-sensitive dye imaging in adult mice reveals that somatosensory maps lost to stroke are replaced over weeks by new structural and functional circuits with prolonged modes of activation within both the peri-infarct zone and distant sites. *J. Neurosci.* 29 (6), 1719–1734.

- Bundo, M., et al., 2002. Changes of neural activity correlate with the severity of cortical ischemia in patients with unilateral major cerebral artery occlusion. *Stroke* 33 (1), 61–66.
- Davalos, D., et al., 2005. ATP mediates rapid microglial response to local brain injury *in vivo*. *Nat. Neurosci.* 8 (6), 752–758.
- Dirnagl, U., Iadecola, C., Moskowitz, M.A., 1999. Pathobiology of ischaemic stroke: an integrated view. *Trends Neurosci.* 22 (9), 391–397.
- Dohmen, C., et al., 2008. Spreading depolarizations occur in human ischemic stroke with high incidence. *Ann. Neurol.* 63 (6), 720–728.
- Dreier, J.P., et al., 2006. Delayed ischaemic neurological deficits after subarachnoid haemorrhage are associated with clusters of spreading depolarizations. *Brain* 129 (Pt 12), 3224–3237.
- Dreier, J.P., 2011. The role of spreading depression: spreading depolarization and spreading ischemia in neurological disease. *Nat. Med.* 17 (4), 439–447.
- Dunn, A.K., et al., 2001. Dynamic imaging of cerebral blood flow using laser speckle. *J. Cereb. Blood Flow Metab.* 21 (3), 195–201.
- Fabricius, M., et al., 2006. Cortical spreading depression and peri-infarct depolarization in acutely injured human cerebral cortex. *Brain* 129 (Pt 3), 778–790.
- Ferron, J.F., et al., 2009. Cortical inhibition during burst suppression induced with isoflurane anesthesia. *J. Neurosci.* 29 (31), 9850–9860.
- Fox, P.T., Raichle, M.E., 1986. Focal physiological uncoupling of cerebral blood flow and oxidative metabolism during somatosensory stimulation in human subjects. *Proc. Natl. Acad. Sci. U.S.A.* 83 (4), 1140–1144.
- Gibbs, J.W., 1898. Fourier's series. *Nature* 59 (1522), 200.
- Hainsworth, A.H., Markus, H.S., 2008. Do *in vivo* experimental models reflect human cerebral small vessel disease? A systematic review. *J. Cereb. Blood Flow Metab.* 28 (12), 1877–1891.
- Hartings, J.A., et al., 2003. Delayed secondary phase of peri-infarct depolarizations after focal cerebral ischemia: relation to infarct growth and neuroprotection. *J. Neurosci.* 23 (37), 11602–11610.
- Hartings, J.A., Tortella, F.C., Rolli, M.L., 2006. AC electrocorticographic correlates of peri-infarct depolarizations during transient focal ischemia and reperfusion. *J. Cereb. Blood Flow Metab.* 26 (5), 696–707.
- Janssen, B.J., et al., 2004. Effects of anesthetics on systemic hemodynamics in mice. *Am. J. Physiol. Heart Circ. Physiol.* 287 (4), H1618–24.
- Jeffcote, T., et al., 2014. Detection of spreading depolarization with intraparenchymal electrodes in the injured human brain. *Neurocrit. Care* 20 (1), 21–31.
- Jeong, J.W., et al., 2015. Soft materials in neuroengineering for hard problems in neuroscience. *Neuron* 86 (1), 175–186.
- Jones, P.B., et al., 2008. Simultaneous multispectral reflectance imaging and laser speckle flowmetry of cerebral blood flow and oxygen metabolism in focal cerebral ischemia. *J. Biomed. Opt.* 13 (4), 044007.
- Kamoun, W.S., et al., 2010. Simultaneous measurement of RBC velocity: flux, hematocrit and shear rate in vascular networks. *Nat. Methods* 7 (8), 655–660.
- Kazmi, S.M., et al., 2013. Chronic imaging of cortical blood flow using Multi-Exposure Speckle Imaging. *J. Cereb. Blood Flow Metab.* 33 (6), 798–808.
- Kazmi, S.M., et al., 2015. Expanding applications: accuracy, and interpretation of laser speckle contrast imaging of cerebral blood flow. *J. Cereb. Blood Flow Metab.* 35 (7), 1076–1084.
- Kozai, T.D., et al., 2014. Chronic tissue response to carboxymethyl cellulose based dissolvable insertion needle for ultra-small neural probes. *Biomaterials* 35 (34), 9255–9268.
- Kozai, T.D., et al., 2016. Two-photon imaging of chronically implanted neural electrodes: sealing methods and new insights. *J. Neurosci. Methods* 258, 46–55.
- Kuzum, D., et al., 2014. Transparent and flexible low noise graphene electrodes for simultaneous electrophysiology and neuroimaging. *Nat. Commun.* 5, 5259.
- Lauritzen, M., 1994. Pathophysiology of the migraine aura. The spreading depression theory. *Brain* 117 (Pt 1), 199–210.
- Li, P., Murphy, T.H., 2008. Two-photon imaging during prolonged middle cerebral artery occlusion in mice reveals recovery of dendritic structure after reperfusion. *J. Neurosci.* 28 (46), 11970–11979.
- Li, P., et al., 2006. Imaging cerebral blood flow through the intact rat skull with temporal laser speckle imaging. *Opt. Lett.* 31 (12), 1824–1826.
- Liu, J., et al., 2015. Syringe-injectable electronics. *Nat. Nanotechnol.* 10 (7), 629–636.
- Luan, L., et al., 2017. Ultraflexible nanoelectronic probes form reliable, glial scar-free neural integration. *Sci. Adv.* 3 (2), e1601966.
- Murphy, T.H., Corbett, D., 2009. Plasticity during stroke recovery: from synapse to behaviour. *Nat. Rev. Neurosci.* 10 (12), 861–872.
- Murphy, T.H., et al., 2016. High-throughput automated home-cage mesoscopic functional imaging of mouse cortex. *Nat. Commun.* 7, 11611.
- Nakamura, H., et al., 2010. Spreading depolarizations cycle around and enlarge focal ischaemic brain lesions. *Brain* 133 (Pt 7), 1994–2006.
- Nishimura, N., et al., 2006. Targeted insult to subsurface cortical blood vessels using ultrashort laser pulses: three models of stroke. *Nat. Methods* 3 (2), 99–108.
- Park, D.W., et al., 2014. Graphene-based carbon-layered electrode array technology for neural imaging and optogenetic applications. *Nat. Commun.* 5, 5258.
- Polikov, V.S., Tresco, P.A., Reichert, W.M., 2005. Response of brain tissue to chronically implanted neural electrodes. *J. Neurosci. Methods* 148 (1), 1–18.
- Ponticorvo, A., Dunn, A.K., 2010. Simultaneous imaging of oxygen tension and blood flow in animals using a digital micromirror device. *Opt. Express* 18 (8), 8160–8170.
- Potter, K.A., et al., 2012. Stab injury and device implantation within the brain results in inversely multiphasic neuroinflammatory and neurodegenerative responses. *J. Neural Eng.* 9 (4), 046020.
- Rousche, P.J., Normann, R.A., 1998. Chronic recording capability of the Utah intracortical electrode array in cat sensory cortex. *J. Neurosci. Methods* 82 (1), 1–15.
- Rumsey, W.L., Vanderkooi, J.M., Wilson, D.F., 1988. Imaging of phosphorescence: a novel method for measuring oxygen distribution in perfused tissue. *Science* 241 (4873), 1649–1651.
- Sakadzic, S., et al., 2010. Two-photon high-resolution measurement of partial pressure of oxygen in cerebral vasculature and tissue. *Nat. Methods* 7 (9), 755–759.
- Schaffer, C.B., et al., 2006. Two-photon imaging of cortical surface microvessels reveals a robust redistribution in blood flow after vascular occlusion. *PLoS Biol.* 4 (2), e22.
- Schrantdt, C.J., et al., 2015. Chronic monitoring of vascular progression after ischemic stroke using multiexposure speckle imaging and two-photon fluorescence microscopy. *J. Cereb. Blood Flow Metab.* 35 (6), 933–942.
- Seymour, J.P., Kipke, D.R., 2007. Neural probe design for reduced tissue encapsulation in CNS. *Biomaterials* 28 (25), 3594–3607.
- Shin, H.K., et al., 2006. Vasoconstrictive neurovascular coupling during focal ischemic depolarizations. *J. Cereb. Blood Flow Metab.* 26 (8), 1018–1030.
- Strong, A.J., et al., 2002. Spreading and synchronous depressions of cortical activity in acutely injured human brain. *Stroke* 33 (12), 2738–2743.
- Strong, A.J., et al., 2006. Evaluation of laser speckle flowmetry for imaging cortical perfusion in experimental stroke studies: quantitation of perfusion and detection of peri-infarct depolarisations. *J. Cereb. Blood Flow Metab.* 26 (5), 645–653.
- Strong, A.J., et al., 2007. Peri-infarct depolarizations lead to loss of perfusion in ischaemic gyrencephalic cerebral cortex. *Brain* 130 (Pt 4), 995–1008.
- Sullender, C.T., Mark, A.E., Clark, T.A., Esipova, T.V., Vinogradov, S.A., Jones, T.A., Dunn, A.K., 2017. Simultaneous Imaging of Oxygen Tension and Cerebral Blood Flow, Manuscript in review.
- Tian, B., et al., 2012. Macroporous nanowire nanoelectronic scaffolds for synthetic tissues. *Nat. Mater.* 11 (11), 986–994.
- Watson, B.D., et al., 1985. Induction of reproducible brain infarction by photochemically initiated thrombosis. *Ann. Neurol.* 17 (5), 497–504.
- Winship, I.R., Murphy, T.H., 2008. In vivo calcium imaging reveals functional rewiring of single somatosensory neurons after stroke. *J. Neurosci.* 28 (26), 6592–6606.
- Woitzik, J., et al., 2013. Propagation of cortical spreading depolarization in the human cortex after malignant stroke. *Neurology* 80 (12), 1095–1102.
- Xie, C., et al., 2015. Three-dimensional macroporous nanoelectronic networks as minimally invasive brain probes. *Nat. Mater.* 14 (12), 1286–1292.
- Zhang, S., Murphy, T.H., 2007. Imaging the impact of cortical microcirculation on synaptic structure and sensory-evoked hemodynamic responses *in vivo*. *PLoS Biol.* 5 (5), e119.
- Zhang, Z., et al., 1997. A new rat model of thrombotic focal cerebral ischemia. *J. Cereb. Blood Flow Metab.* 17 (2), 123–135.
- Zhong, Y., Bellamkonda, R.V., 2008. Biomaterials for the central nervous system. *J. R. Soc. Interface* 5 (26), 957–975.